Imaging cone photoreceptors in three dimensions and in time using ultrahigh resolution optical coherence tomography with adaptive optics

Omer P. Kocaoglu,* Sangyeol Lee, Ravi S. Jonnal, Qiang Wang, Ashley E. Herde, Jack C. Derby, Weihua Gao, and Donald T. Miller

School of Optometry, Indiana University, 800 East Atwater Avenue, Bloomington, IN 47405, USA
*okocaogl@indiana.edu

Abstract: Cone photoreceptors in the living human eye have recently been imaged with micron-scale resolution in all three spatial dimensions using adaptive optics optical coherence tomography. While these advances have allowed non-invasive study of the three-dimensional structure of living human cones, studies of their function and physiology are still hampered by the difficulties to monitor the same cells over time. The purpose of this study is to demonstrate the feasibility of cone monitoring using ultrahigh-resolution adaptive optics optical coherence tomography. Critical to this is incorporation of a high speed CMOS camera (125 KHz) and a novel feature-based, image registration/dewarping algorithm for reducing the deleterious effects of eye motion on volume images. Volume movies were acquired on three healthy subjects at retinal eccentricities from 0.5° to 6°. Image registration/dewarping reduced motion artifacts in the movies from 15 μm to 1.3 μm root mean square, the latter sufficient for identifying and tracking cones. Cone row-to-row spacing and outer segment lengths were consistent with that reported in the literature. Cone length analysis demonstrates that UHR-AO-OCT is sufficiently sensitive to measure real length differences between cones in the same 0.5° retinal patch, and requires no more than five measurements of OS length to achieve 95% confidence. We know of no other imaging modality that can monitor foveal or parafoveal cones over time with comparable resolution in all three dimensions.

References and links:

1. M. Wojtkowski, R. Leitgeb, A. Kowalczyk, T. Bajraszewski, and A. F. Fercher, "In vivo human retinal imaging by Fourier domain optical coherence tomography," J. Biomed. Opt. **7**(3), 457–463 (2002).
2. B. Cense, N. Nassif, T. Chen, M. Pierce, S. H. Yun, B. Park, B. Bouma, G. Tearney, and J. de Boer, "Ultrahigh-resolution high-speed retinal imaging using spectral-domain optical coherence tomography," Opt. Express **12**(11), 2435–2447 (2004).
3. M. Wojtkowski, V. Srinivasan, J. G. Fujimoto, T. Ko, J. S. Schuman, A. Kowalczyk, and J. S. Duker, "Three-dimensional retinal imaging with high-speed ultrahigh-resolution optical coherence tomography," Ophthalmology **112**(10), 1734–1746 (2005).
4. Y. Zhang, J. Rha, R. Jonnal, and D. T. Miller, "Adaptive optics parallel spectral domain optical coherence tomography for imaging the living retina," Opt. Express **13**(12), 4792–4811 (2005).
5. E. J. Fernández, B. Povazay, B. Hermann, A. Unterhuber, H. Sattmann, P. M. Prieto, R. Leitgeb, P. Ahnelt, P. Artal, and W. Drexler, "Three-dimensional adaptive optics ultrahigh-resolution optical coherence tomography using a liquid crystal spatial light modulator," Vision Res. **45**(28), 3432–3444 (2005).

6. R. J. Zawadzki, S. M. Jones, S. S. Olivier, M. Zhao, B. A. Bower, J. A. Izatt, S. Choi, S. Laut, and J. S. Werner, "Adaptive-optics optical coherence tomography for high-resolution and high-speed 3D retinal in vivo imaging," Opt. Express **13**(21), 8532–8546 (2005).
7. Y. Zhang, B. Cense, J. Rha, R. S. Jonnal, W. Gao, R. J. Zawadzki, J. S. Werner, S. Jones, S. Olivier, and D. T. Miller, "High-speed volumetric imaging of cone photoreceptors with adaptive optics spectral-domain optical coherence tomography," Opt. Express **14**(10), 4380–4394 (2006).
8. D. Merino, C. Dainty, A. Bradu, and A. G. Podoleanu, "Adaptive optics enhanced simultaneous en-face optical coherence tomography and scanning laser ophthalmoscopy," Opt. Express **14**(8), 3345–3353 (2006).
9. C. E. Bigelow, N. V. Iftimia, R. D. Ferguson, T. E. Ustun, B. Bloom, and D. X. Hammer, "Compact multimodal adaptive-optics spectral-domain optical coherence tomography instrument for retinal imaging," J. Opt. Soc. Am. A **24**(5), 1327–1336 (2007).
10. R. J. Zawadzki, S. S. Choi, S. M. Jones, S. S. Oliver, and J. S. Werner, "Adaptive optics-optical coherence tomography: optimizing visualization of microscopic retinal structures in three dimensions," J. Opt. Soc. Am. A **24**(5), 1373–1383 (2007).
11. R. J. Zawadzki, B. Cense, Y. Zhang, S. S. Choi, D. T. Miller, and J. S. Werner, "Ultrahigh-resolution optical coherence tomography with monochromatic and chromatic aberration correction," Opt. Express **16**(11), 8126–8143 (2008).
12. E. J. Fernández, B. Hermann, B. Považay, A. Unterhuber, H. Sattmann, B. Hofer, P. K. Ahnelt, and W. Drexler, "Ultrahigh resolution optical coherence tomography and pancorrection for cellular imaging of the living human retina," Opt. Express **16**(15), 11083–11094 (2008).
13. B. Cense, E. Koperda, J. M. Brown, O. P. Kocaoglu, W. Gao, R. S. Jonnal, and D. T. Miller, "Volumetric retinal imaging with ultrahigh-resolution spectral-domain optical coherence tomography and adaptive optics using two broadband light sources," Opt. Express **17**(5), 4095–4111 (2009).
14. C. Torti, B. Považay, B. Hofer, A. Unterhuber, J. Carroll, P. K. Ahnelt, and W. Drexler, "Adaptive optics optical coherence tomography at 120,000 depth scans/s for non-invasive cellular phenotyping of the living human retina," Opt. Express **17**(22), 19382–19400 (2009).
15. B. Cense, W. Gao, J. M. Brown, S. M. Jones, R. S. Jonnal, M. Mujat, B. H. Park, J. F. de Boer, and D. T. Miller, "Retinal imaging with polarization-sensitive optical coherence tomography and adaptive optics," Opt. Express **17**(24), 21634–21651 (2009).
16. E. J. Fernández, A. Unterhuber, B. Považay, B. Hermann, P. Artal, and W. Drexler, "Chromatic aberration correction of the human eye for retinal imaging in the near infrared," Opt. Express **14**(13), 6213–6225 (2006).
17. S. Martinez-Conde, S. L. Macknik, and D. H. Hubel, "The role of fixational eye movements in visual perception," Nat. Rev. Neurosci. **5**(3), 229–240 (2004).
18. B. Potsaid, I. Gorczynska, V. J. Srinivasan, Y. Chen, J. Jiang, A. Cable, and J. G. Fujimoto, "Ultrahigh speed spectral / Fourier domain OCT ophthalmic imaging at 70,000 to 312,500 axial scans per second," Opt. Express **16**(19), 15149–15169 (2008).
19. T. Schmoll, C. Kolbitsch, and R. A. Leitgeb, "Ultra-high-speed volumetric tomography of human retinal blood flow," Opt. Express **17**(5), 4166–4176 (2009).
20. S. B. Stevenson and A. Roorda, "Correcting for miniature eye movements in high resolution scanning laser ophthalmoscopy," in Proc. SPIE **5688** 145 (2005)
21. D. X. Hammer, R. D. Ferguson, C. E. Bigelow, N. V. Iftimia, T. E. Ustun, and S. A. Burns, "Adaptive optics scanning laser ophthalmoscope for stabilized retinal imaging," Opt. Express **14**(8), 3354–3367 (2006).
22. C. R. Vogel, D. W. Arathorn, A. Roorda, and A. Parker, "Retinal motion estimation in adaptive optics scanning laser ophthalmoscopy," Opt. Express **14**(2), 487–497 (2006).
23. T. Y. Chui, H. Song, and S. A. Burns, "Adaptive-optics imaging of human cone photoreceptor distribution," J. Opt. Soc. Am. A **25**(12), 3021–3029 (2008).
24. T. Y. Chui, H. Song, and S. A. Burns, "Individual variations in human cone photoreceptor packing density: variations with refractive error," Invest. Ophthalmol. Vis. Sci. **49**(10), 4679–4687 (2008).
25. Q. Yang, D. W. Arathorn, P. Tiruveedhula, C. R. Vogel, and A. Roorda, "Design of an integrated hardware interface for AOSLO image capture and cone-targeted stimulus delivery," Opt. Express **18**(17), 17841–17858 (2010).
26. R. S. Jonnal, J. R. Besecker, J. C. Derby, O. P. Kocaoglu, B. Cense, W. Gao, Q. Wang, and D. T. Miller, "Imaging outer segment renewal in living human cone photoreceptors," Opt. Express **18**(5), 5257–5270 (2010).
27. J. Rha, R. S. Jonnal, K. E. Thorn, J. Qu, Y. Zhang, and D. T. Miller, "Adaptive optics flood-illumination camera for high speed retinal imaging," Opt. Express **14**(10), 4552–4569 (2006).
28. M. Pircher, B. Baumann, E. Götzinger, H. Sattmann, and C. K. Hitzenberger, "Simultaneous SLO/OCT imaging of the human retina with axial eye motion correction," Opt. Express **15**(25), 16922–16932 (2007).
29. M. Pircher, E. Götzinger, H. Sattmann, R. A. Leitgeb, and C. K. Hitzenberger, "In vivo investigation of human cone photoreceptors with SLO/OCT in combination with 3D motion correction on a cellular level," Opt. Express **18**(13), 13935–13944 (2010).
30. D. T. Miller, D. R. Williams, G. M. Morris, and J. Liang, "Images of cone photoreceptors in the living human eye," Vision Res. **36**(8), 1067–1079 (1996).
31. O. P. Kocaoglu, B. Cense, Q. Wang, J. Bruestle, J. Besecker, W. Gao, R. Jonnal, and D. T. Miller, "Imaging retinal nerve fiber bundles at ultrahigh-speed and ultrahigh-resolution using OCT with adaptive optics," Proc. SPIE **7550**(755010), 755010, 755010-5 (2010).

32. ANSI Z136, 1 "Safe use of lasers" (Laser Institute of America, 2007).
33. W. S. Rasband, "ImageJ" (U.S. National Institutes of Health, Bethesda, Maryland, 1997–2009) http://rsb.info.nih.gov/ij/.
34. T. H. Cormen, C. E. Leiserson, R. L. Rivest, and C. Stein, *Introduction to Algorithms*, 2nd ed. (MIT Press, 2001).
35. J. I. Yellott, Jr., "Spectral analysis of spatial sampling by photoreceptors: topological disorder prevents aliasing," Vision Res. **22**(9), 1205–1210 (1982).
36. A. W. Snyder and C. Pask, "The Stiles-Crawford effect--explanation and consequences," Vision Res. **13**(6), 1115–1137 (1973).
37. C. A. Curcio, K. R. Sloan, Jr., O. Packer, A. E. Hendrickson, and R. E. Kalina, "Distribution of cones in human and monkey retina: individual variability and radial asymmetry," Science **236**(4801), 579–582 (1987).
38. L. A. Riggs, J. C. Armington, and F. Ratliff, "Motions of the retinal image during fixation," J. Opt. Soc. Am. **44**(4), 315–321 (1954).
39. J. Liang, D. R. Williams, and D. T. Miller, "Supernormal vision and high-resolution retinal imaging through adaptive optics," J. Opt. Soc. Am. A **14**(11), 2884–2892 (1997).
40. V. J. Srinivasan, B. K. Monson, M. Wojtkowski, R. A. Bilonick, I. Gorczynska, R. Chen, J. S. Duker, J. S. Schuman, and J. G. Fujimoto, "Characterization of outer retinal morphology with high-speed, ultrahigh-resolution optical coherence tomography," Invest. Ophthalmol. Vis. Sci. **49**(4), 1571–1579 (2008).
41. J. T. McAllister, A. M. Dubis, D. M. Tait, S. Ostler, J. Rha, K. E. Stepien, C. G. Summers, and J. Carroll, "Arrested development: high-resolution imaging of foveal morphology in albinism," Vision Res. **50**(8), 810–817 (2010).

1. Introduction

Spectral domain optical coherence tomography (SD-OCT) is an *in vivo* imaging modality capable of axially resolving cellular layers in the living retina [1–3]. Three dimensional cellular imaging, however, also requires resolving cells in the two lateral dimensions. Unlike axial resolution, lateral resolution of SD-OCT is limited by the quality of the eye's optics (monochromatic and chromatic aberrations) and beam diameter at the eye's pupil (diffraction). All three effects increase spot size at the retina and limit the ability of SD-OCT to image the 3D retina at the cellular level. A strategy that has been successfully employed to correct monochromatic aberrations across a large pupil (>6 mm) in SD-OCT is adaptive optics (AO) [4–15]. Correction of the longitudinal chromatic aberrations over the spectral bandwidth of the SD-OCT light source has been accomplished with a custom achromatizing lens [16,11]. In combination, ultrahigh-resolution SD-OCT systems with adaptive optics (UHR-AO-OCT) and an achromatizing lens have been reported to achieve diffraction limited imaging of the retina with a volume resolution of 3x3x3 μm^3. This performance allows three-dimensional imaging of cellular structures in the retina [11–14]. Functional imaging of these same structures and their underlying physiology, however, requires the additional dimension of time, i.e., the ability to track and monitor temporal changes in the same cells across frames of AO-OCT videos.

All *in vivo* retinal imaging techniques suffer the effects of involuntary eye movements that occur even under normal fixation, such as tremor, drift, and microsaccades [17]. The resulting image blur and distortion diminish the visibility of retinal structures. Efforts at functional imaging suffer a third repercussion, as eye movements also complicate the process of tracking these structures over time. Recently, the use of CMOS line-scan cameras in the SD-OCT detection channel has resulted in acquisition speeds up to 312.5K lines/s [18,19,14]. While increased acquisition speed significantly reduces motion artifacts within volumes and feature displacement between volumes, it does not completely eliminate them. Further improvement can be gained using additional hardware, e.g., dynamic retinal tracking, and software, e.g., registration/dewarping algorithms–methodologies that have been successfully applied to other retinal imaging modalities for single cell imaging. For example, AO-SLO [20–25] and AO flood-illumination [26,27] cameras combined with dynamic retinal tracking and/or post processing correction for motion artifacts have been successfully used to image cone photoreceptors. Both camera methodologies have captured exquisite details of the cone apertures *en face*, though fail with the corresponding depth information of the cone structure owing to their relatively poor axial resolution (>60 μm).

In recent years cone photoreceptors have been imaged with a variety of OCT configurations: OCT [28,18,29], AO-OCT [7,10], and UHR-AO-OCT [11–14] OCT studies rely primarily on high-speed imaging to reduce motion artifacts, but without AO, are limited to eccentricities relatively distant from the fovea (greater than ~4°), where cones are comparatively large and widely spaced, and eyes endowed with good optics. This strategy parallels that used for the first observations of individual cones in the living human retina [30]. AO-OCT and UHR-AO-OCT do not share these limitations. Both have been used in early studies of the three-dimensional structure of cones, but more detailed and exhaustive studies have largely been impractical because of eye motion artifacts that prevent tracking of individual cones. Successful tracking would allow AO-OCT studies of the fast physiological processes that accompany phototransduction in individual photoreceptors and the much slower ones of disc renewal and phagocytosis. These are critical for normal photoreceptor function and are known to be disrupted by retinal disease such as age-related macular degeneration and retinitis pigmentosa.

In this study, we combined three critical tools to achieve three-dimensional imaging of cone photoreceptors over time: (1) a UHR-AO-OCT system to resolve in all three dimensions cone photoreceptors, (2) a high speed CMOS line-scan camera for fast image acquisition to decrease motion artifacts and subsequent image degradation, and (3) a feature-based registration/dewarping algorithm to decrease further the motion artifacts. To assess the effectiveness of this combination, we imaged cone photoreceptors of three healthy subjects at several retinal eccentricities temporal to the fovea, and analyzed the volume videos in both *en face* and cross-section. We quantified the improvement in terms of reduced eye motion artifacts and improved cone contrast. As supportive evidence of cone visualization and monitoring, cone spacing as well as outer segment (OS) lengths were measured (in some cases repeatedly) and compared to the literature.

2. Materials and methods

2.1. UHR-AO-OCT system

A detailed description of an earlier version of the UHR-AO-OCT system can be found in Zhang *et al.* [7] and in Cense *et al.* [13]. In brief, the system consists of a fiber-based SD-OCT sub-system that uses a spectrally broadband light source for increased axial resolution and a woofer-tweeter AO sub-system for increased lateral resolution. The OCT light source is a BroadLighter T840 from Superlum, Inc ($\Delta\lambda$ = 110 nm, λ_c = 840 nm, P = 12 mW). The woofer-tweeter is two wavefront correctors, a 37-electrode bimorph mirror from AOptix Technologies, Inc. (AOptix) and a 140-discrete-actuator deformable mirror from Boston Micromachines Corporation (BMC). Both correctors are positioned conjugate to the subject's pupil. The UHR-AO-OCT system achieves a 3D resolution of 3x3x3 μm^3 in retinal tissue, as shown in Cense *et al.* [13]. The critical hardware improvement for this study is the integration of a high-speed CMOS line-scan detector (Basler Sprint, Exton PA) in the detection channel of the SD-OCT sub-system. The CMOS detector contains two 10 μm, 4096-pixel lines that were vertically binned, producing an effective pixel size of 10x20 μm^2. The full spectrum was detected by using the central 2048 pixels of the CMOS camera, which allowed acquisition of OCT images at a speed of 125K lines/s. This speed was found empirically to be a reasonable compromise between signal-to-noise ratio and motion artifacts based on retinal imaging at different acquisition rates with the CMOS detector [31]. Also for this study, the OCT control and acquisition software was upgraded to a 64-bit platform and recoded in C# and C++ for increased volume acquisition and storage, faster processing, and enhanced user control.

2.2. Experiment

We acquired UHR-AO-OCT volume movies of 0.5° x 0.5° (150 x 150 μm) retinal patches consisting of 15 volumes with 1 μm spacing between successive A-scans and B-scans in ~2.7

seconds. Images were acquired at five retinal locations (0.5°, 1.5°, 3°, 4.5°, and 6° temporal to the fovea) by having the subject fixate at different points along a self-illuminated target (liquid crystal display) with the eye being imaged. The five retinal eccentricities covered a wide range of cone sizes and packing densities. Of these locations, three (1.5°, 3°, and 6°) were selected for analysis as described below in Section 2.3.

Operation of the woofer-tweeter AO system during the experiment entailed sequential control of the AOptix and BMC mirrors. Best correction of the AOptix mirror was determined first, then the BMC. Once a stable maximum strehl ratio was reached (typically > 0.8 as measured by the wavefront sensor), dynamic correction with the BMC continued at approximately 19.1 Hz during which UHR-AO-OCT images of the retina were acquired. The large stroke of the AOptix mirror was also used to position system focus at the cone photoreceptor layer. Coarse adjustment in focus was guided by image quality of the UHR-AO-OCT image displayed in real time on the computer monitor. Fine adjustment of focus entailed acquiring a series of UHR-AO-OCT images of the same patch of retina with slightly different focus (typically +/− 0.05 Diopters) to ensure that clear images (visual determination) of the photoreceptor layer were obtained. This two-step focus procedure (coarse and fine) minimized the impact of focus error on the clarity of individual cones, the retinal layer of interest in this study. The two-step procedure was repeated for each retinal eccentricity and subject imaged.

Three subjects were imaged. All had best corrected visual acuity of 20/20 or better and were free of ocular disease. The subjects' age, refractive error, visual acuity and axial length are listed in Table 1. All procedures adhered to the tenets of the Helsinki Declaration and the Institutional Review Board of Indiana University. The maximum power delivered to the eye was 400µW, measured at the cornea and within the safety limits established by ANSI [32]. The subject's eye was dilated and cyclopleged using a 0.5% Tropicamide drop. A bite bar mounted on a motorized, joystick-controlled XYZ translation stage was used to stabilize the subject's head and position the pupil.

Table 1. List of subjects' age, refractive error, best-corrected visual acuity, and axial length[a]

Subject	Age (y)	Refractive error (D)	Visual acuity (letter)	Axial length (mm)
1	32	−3 S	20/10	26.06
2	28	Plano	20/15	23.78
3	23	Plano	20/20	23.55

[a]Eye length was measured with the Zeiss IOLMaster®. All ocular parameters are for the subjects' right eye.

2.3. Post processing: registration/dewarping of UHR-AO-OCT volumes

As expected, volumetric UHR-AO-OCT movies of the retina suffered from eye motion artifacts in all spatial dimensions. Lateral motion artifacts were found more challenging to remove than the axial ones, due to their manifestation as both translational motion artifacts between volumes and as warping within volumes. Removal of lateral and axial motion artifacts was done separately (first axial, than lateral) using semi-automated registration algorithms implemented as Java plugins (extensions) for ImageJ [33], a public domain Java image processing and analysis program. Effectiveness of the registration/dewarping was quantified by measuring the extent of the motion artifacts before and after application of the ImageJ plugins. Details of both steps (first removal of motion artifacts, then effectiveness to do so) are described next.

UHR-AO-OCT volumes were registered axially first. To start, the connecting cilia (CC) layer was identified and then segmented using a dynamic programming algorithm [34]. The algorithm identifies the CC layer using a Hessian blob orientation detector combined with a path cost minimization algorithm for smoothing. Once segmented, fast B-scans were axially

shifted to flatten the CC layer (see Fig. 1). Here we treated each fast B-scan as a rigid body (assume no motion artifacts), a reasonable approximation as each was collected in just 1.3 ms. Finally, the photoreceptor layer and retinal pigment epithelium (PL-RPE) complex was extracted from the axially registered volumes and *en face* projections generated.
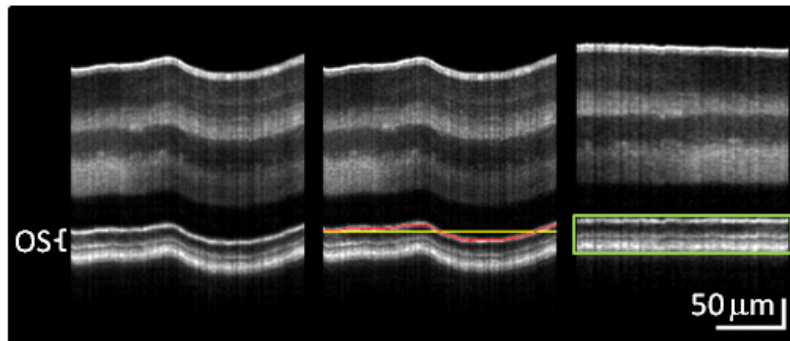

Fig. 1. Procedure for axially registering UHR-AO-OCT volume movies. Shown is a projected slow B-scan (each column is the average of a single fast B-scan) at various stages of the process: (left) before axial registration; (center) segmentation of CC (red line) and determination of its mean height (yellow line); and (right) axial shifting of fast B-scans to align CC (red line in (center)) to their mean height (yellow line in (center)). Green rectangle denotes the region of interest (PL and RPE complex) that is cropped and used for further processing. OS: outer segment of cone photoreceptors.

Next, the extracted volumes were registered/dewarped laterally. To start, volumes with excessive motion artifacts (as for example from a microsaccade) were removed from the movie. The number of frames dropped in any given video was no more than three (out of 15 total frames). The one exception was the video at 1.5° for subject #3 (S3) in which seven frames were dropped. For this particular video, the subject did not fixate well. The *en face* view of each volume was then used to manually identify ten to 15 landmark cones that were strategically chosen to be roughly evenly distributed in the slow scan direction of the volume (see Fig. 2 (left)). Distribution of selected cones along the fast scan direction was largely inconsequential to the registration process owing to the fast acquisition time (1.3 ms per B-scan). Preference was therefore given to cones that were clear and punctate. The locations of landmark cone centers were manually tracked and recorded through the volume movie by a trained specialist.

Next, the *en face* frames were registered/dewarped (Fig. 2) using the landmark cone locations and a customized feature-based registration algorithm. The latter split the *en face* views into strips running the length of the fast scan direction and bordered in the slow scan direction by two landmark cones (Fig. 2 (center)). The 10 to 15 landmark cones generated 9 to 14 strips, each roughly containing 10 to 15 B-scans. The edge B-scans are shared between adjacent strips. This assured continuity across strips and minimized the possibility of artifacts along the strip edges. As each B-scan was acquired in 1.3 ms, each strip was acquired in about 13 to 20 ms. Dewarping consisted of aligning the landmark cone positions to reference positions as defined by the first *en face* frame in the movie that had little to no apparent motion artifacts. While we did not account for warping that might be present in the reference frame, this had little consequence for our application. Tracking individual cones over time is sensitive to relative warp (i.e., between UHR-AO-OCT volumes), not absolute warp. Alignment of landmark cone positions to reference positions was accomplished with two linear transformations: scaling (shrinking and expanding) in slow scan direction and shearing in fast scan direction. The dewarped strips were then reassembled to form an *en face* frame (Fig. 2 (right)). For improved visualization of cones, high spatial frequency noise in the *en face* images was reduced using a low-pass filter with a cutoff of two pixels (2 µm), which is

smaller than the lateral resolution of the UHR-AO-OCT system (3 μm). Single cones were then selected from the volume videos and displayed in *en face* and cross-sectional views.
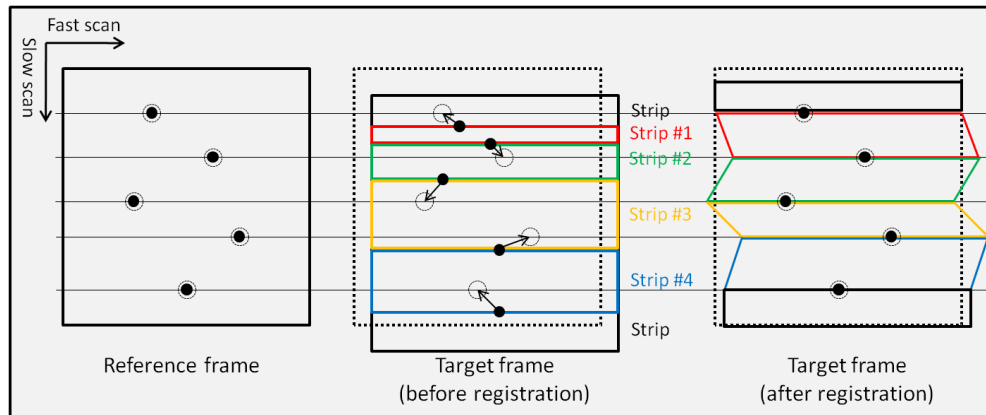

Fig. 2. Procedure for lateral registration of cone photoreceptors in *en face* projections from UHR-AO-OCT volumes. ●: landmark cones, ○: reference positions of landmark cones. (left) Landmark cones are selected and their reference positions determined in the first frame of the movie that had little to no apparent motion artifacts. (center) Each subsequent frame in the volume movie is segmented into 10 to 15 narrow strips whose long dimension is parallel to the fast scan direction. The border of each strip is defined by two landmark cones. (right) To register a strip, landmark cones are repositioned to their original (reference) positions using two linear transformations: scaling (shrinking and expanding) in slow scan direction and shearing in fast scan direction. After registration of the strips, the strips are reassembled to form a registered image. Note that the top and bottom strips are not registered as two landmark cones are needed to do so. The registration process is fully automated once the landmark cone coordinates are found. See text for additional details.

To assess effectiveness of the registration/dewarping methodology, frames within the same videos were averaged and cone contrast measured before and after registration/dewarping. This analysis was applied to volume movies acquired at 1.5°, 3°, and 6° eccentricities for one subject. A second analysis measured the lateral motion of individual cones (ten non-landmark cones and one landmark cone as a control) before and after registration/dewarping. This analysis was applied to volume videos at 3° eccentricity for all three subjects. The average row-to-row spacing of cones was measured at the three retinal eccentricities (1.5°, 3°, and 6°) and for the three subjects based on Yellott's ring [35] in the power spectra. Yellott's ring corresponds to the cone sampling frequency, which is the reciprocal of row-to-row cone spacing. Spacing was compared to measurements in the literature (histology and imaging with an AO scanning laser ophthalmoscope). To assess precision to which individual cone OS lengths can be measured in repeated UHR-AO-OCT volumes of the same video, four cones were selected at each of the three retinal eccentricities (1.5°, 3°, and 6°) and for the three subjects. 36 cones were measured in total with 10 to 15 (14.2, on average) OS length measurements per cone (one measurement per volume in each volume video). The OS length was defined as the distance from the peak of the bright reflection representing CC to the peak of the bright reflection at the posterior OS tip (PTOS). As numerous A-lines sampled the cone aperture, the OS length was measured on the A-line that generated the brightest pixel in the *en face* projection of each cone. The eight A-lines (spaced 1 μm apart) neighboring the A-line of measurement were then checked for potential inconsistencies in brightness. No such inconsistencies were observed for the data sets used in this study. As UHR-AO-OCT measures optical path length (not physical length), we assumed a refractive index of the OS of $n_{os} = 1.43$ in all subjects [36].

3. Results

3.1. Cone spacing measurements

AO correction allowed the resolution of cones as close as 0.5 deg to the fovea. Figure 3 shows representative *en face* images of the axially registered PL-RPE complex for retinal eccentricities of 0.5°, 1.5°, 3°, 4.5°, and 6° temporal to the fovea. The complex was extracted
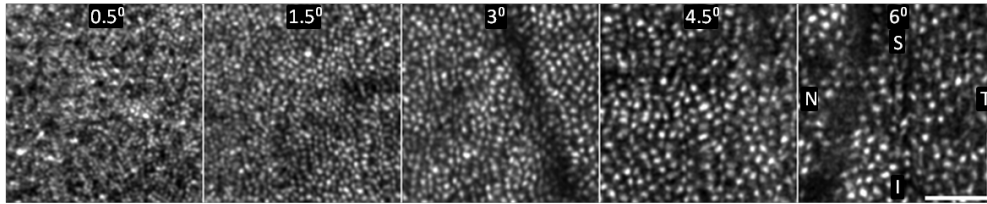

Fig. 3. Representative *en face* images of cone photoreceptors of S3 at 0.5°, 1.5°, 3°, 4.5°, and 6° temporal to the fovea. Scale bars indicate 50 μm. N, T, S, and I denote nasal, temporal, superior, and inferior directions at the retina.
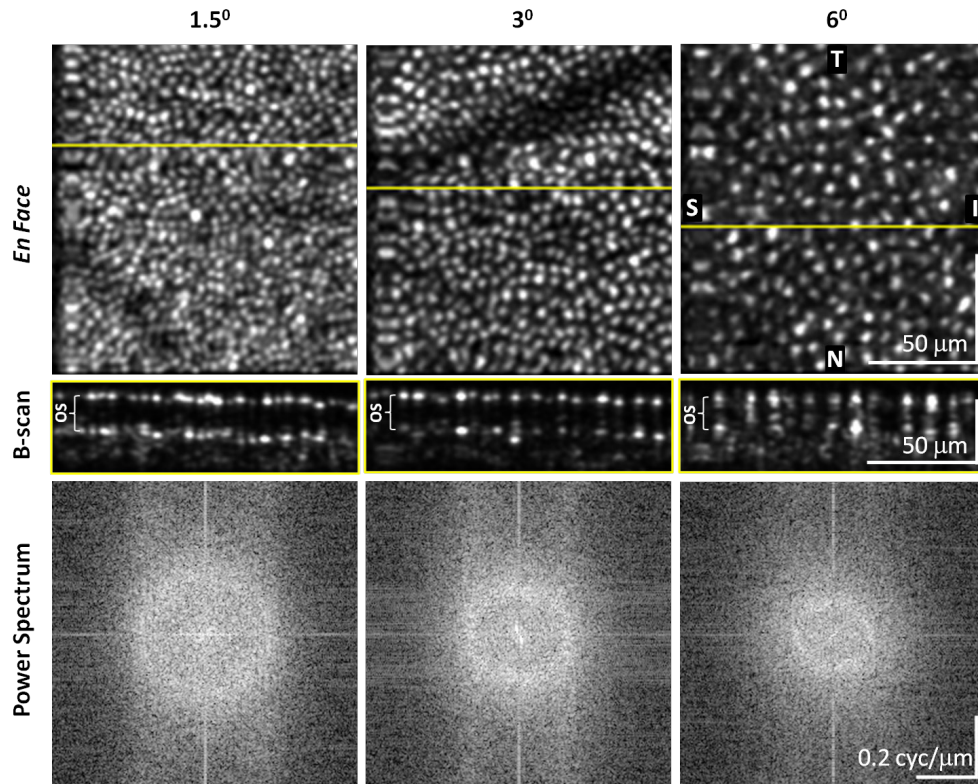
Fig. 4. (top row) Cone photoreceptor images of S3 at 1.5°, 3°, and 6° temporal to the fovea. N, T, S, and I denote nasal, temporal, superior, and inferior directions at the retina. (middle row) Cross-sectional images (fast B-scans) of the PL-RPE complex are shown for the same three retinal eccentricities with location indicated by the yellow lines on the *en face* images. Media 1 shows movie versions that depict the yellow lines sliding on the *en face* images and corresponding B-scans for the entire UHR-AO-OCT volumes. (bottom row) Power spectra were computed from the corresponding *en face* images. Rings of concentrated power and centered on zero spatial frequency are visible. Note that the *en face* images (top row) are rotated 90° relative to the images in Fig. 3. The rotation was necessary for alignment to the fast B-scans (middle row).

from individual volumes of S3. Images reveal a monotonic increase in coarseness (size and separation of bright spots) with retinal eccentricity, the same general trend characteristic of cone photoreceptors. Due to the large number of volumes acquired and the detailed processing undertaken, analysis of the cones (bright spots) was limited to three of the retinal locations (1.5°, 3°, and 6°).

Figure 4 (top row) shows *en face* views of the axially registered PL-RPE complex for the same subject at 1.5°, 3°and 6° temporal to the fovea. The middle row shows cross-sectional images of the PL-RPE complex, the locations of which are indicated with yellow lines in the *en face* view. The cross-sectional images reveal two rows of punctated bright spots that straddle the cone OS. Media 1 that accompanies the figure shows the associated *en face* and cross-sectional movies (149 frames each) of the same retinal patches. Both views reveal a monotonic increase in cone (bright spot) size and spacing with retinal eccentricity. Figure 4 (bottom) shows power spectra of the *en face* views. Rings of concentrated power are visible in the power spectra and have radii that correspond to row-to-row spacing of 4.7 μm, 6.4 μm and 8.3 μm for 1.5°, 3° and 6°, respectively. Figure 5 plots the reciprocal of ring radius as a function of retinal eccentricity for all three subjects. Included for comparison are measurements of cone spacing from Curcio *et al.* [37] and Chui *et al.* [24].
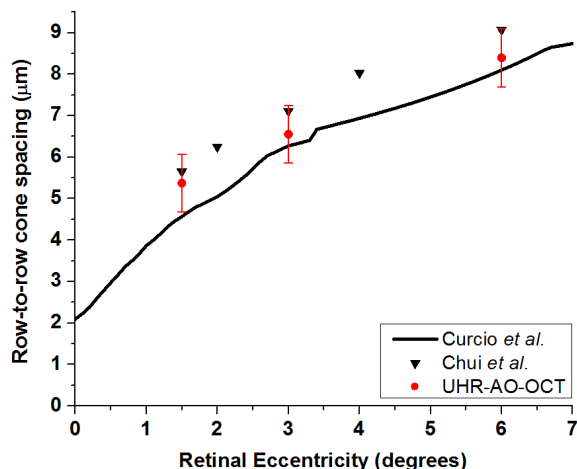

Fig. 5. Comparison of cone photoreceptor spacing measured with UHR-AO-OCT, AO-SLO [24], and histology [37]. All measurements are temporal of the fovea. Error bars represent ± 1 standard deviation.

3.2. Comparison of registered and unregistered en face cone images

Figure 6 and Media 2 show averaged *en face* cone images of S3 at 3 degrees temporal to the fovea with and without registration/dewarping. Two registration/dewarping results are shown, one based on three strips (four landmark cones) and the other 13 strips (14 landmark cones). Averaging was across all e*n face* images of the same volume video (15 images). Without registration/dewarping (Fig. 6 (left)), averaging severely degrades cone clarity in the image, an obvious indicator of the severity of cone misregistration between frames due to eye motion. Average cone contrast (Michelson contrast based on maximum cone reflectance and minimum surround reflectance) is 0.20 ± 0.09 for the retina portion common in all frames. Figure 6 (center) and 6 (right) clearly show that our registration/dewarping methodology preserves cone visibility over most of the image after averaging, indicative of effective cone registration. As evident in the figure, our methodology performs better with more strips (or equivalently more landmark cones), enabling more effective registration of cones over a larger field of view. Average cone contrast is 0.42 ± 0.09 and 0.59 ± 0.07 for three and 13 strips, respectively, for the retina portion common in all frames.
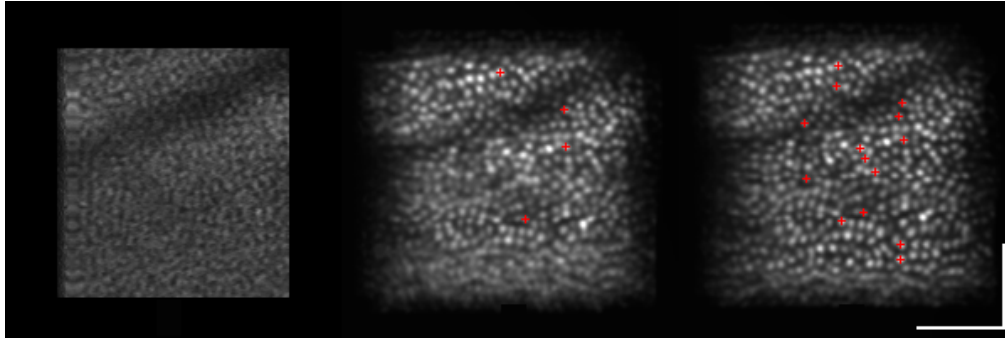
Fig. 6. Average of 15 0.5°x0.5° *en face* images from the same volume video (left) before and (center and right) after registration/dewarping. Images were acquired from subject S3 at 3° temporal to the fovea. Registration/dewarping was based on (center) three subframe strips (4 landmark cones marked with red crosses) and (right) 13 subframe strips (14 landmark cones marked with red crosses). Media 2 shows the corresponding movie versions of each image. Scale bars indicate 50 μm.
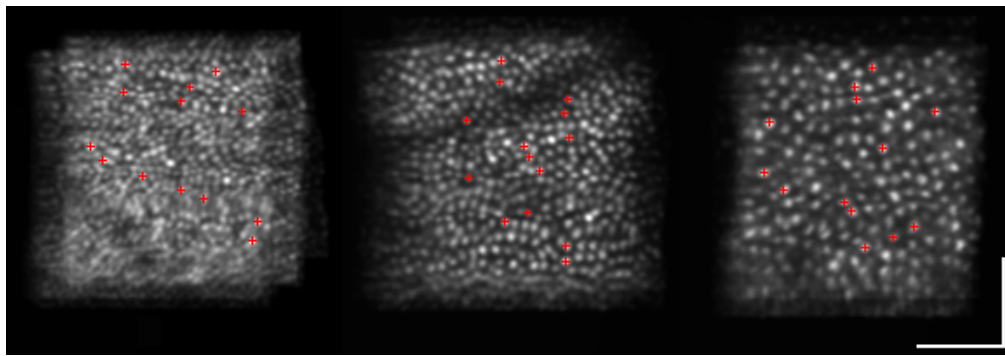

Fig. 7. Average of 15 e*n face* images from the same volume movies of S3 at (left) 1.5°, (center) 3°, and (right) 6° temporal to the fovea after registration/dewarping. Registration/dewarping was based on (left) 12, (center) 13, and (right) 12 subframe strips (13, 14, and 13 landmark cones, respectively). Media 3 shows the registered *en face* UHR-AO-OCT movies from which the average images were computed. Retinal motion for the three videos are comparable with an *en face* motion RMS of 2.2 μm, 1.2 μm, 0.97 μm for 1.5°, 3°, and 6°, respectively. For comparison, RMS retinal motion before registration were 14.4 μm, 14.7 μm, 10.6 μm. Scale bars indicate 50 μm.

Figure 7 and Media 3 extend the registration analysis to the other two retinal eccentricities (1.5° and 6° temporal to the fovea). The figure shows averaged *en face* cone images of S3 at 1.5°, 3°, and 6° after registration using 12, 13, and 12 strips (or equivalently 13, 14, and 13 land mark cones, respectively). Cones are readily apparent after registration/dewarping and averaging, demonstrating the robustness of our methodology to dewarp cones of varying size and packing density. Of course critical to this is finding landmark cones that are distributed along the entire slow scan direction of the image. This did not occur near the bottom of Fig. 7 (left) and resulted in poor registration as evident by reduced cone clarity. Figure 8 quantifies the extent of the retina motion in the *en face* cone movies and the effectiveness of our strip-based registration/dewarping methodology to remove it. Figure 8 (left) shows the cone mosaic projection of a single frame with landmark cones used for registration/dewarping marked with red plus signs and cones used for motion analysis marked with color-coded squares. One landmark cone and 10 non-landmark cones are shown in the *en face* image. Figure 8 (center) traces the movement of these cones during acquisition of the movie. Total motion of any single cone is approximately 55 μm (11 arc min) and corresponds to a root mean square (RMS) of 15 μm (3 arc min). Figure 8 (right) shows the effectiveness of the

registration/dewarping algorithm to reduce the motion of these same cones. The landmark cone is rendered motionless (by definition), while the non-landmark cones are greatly stabilized. Stabilized cones have a residual motion of approximately 1.3 µm RMS, noticeably less than the width of an individual cone.
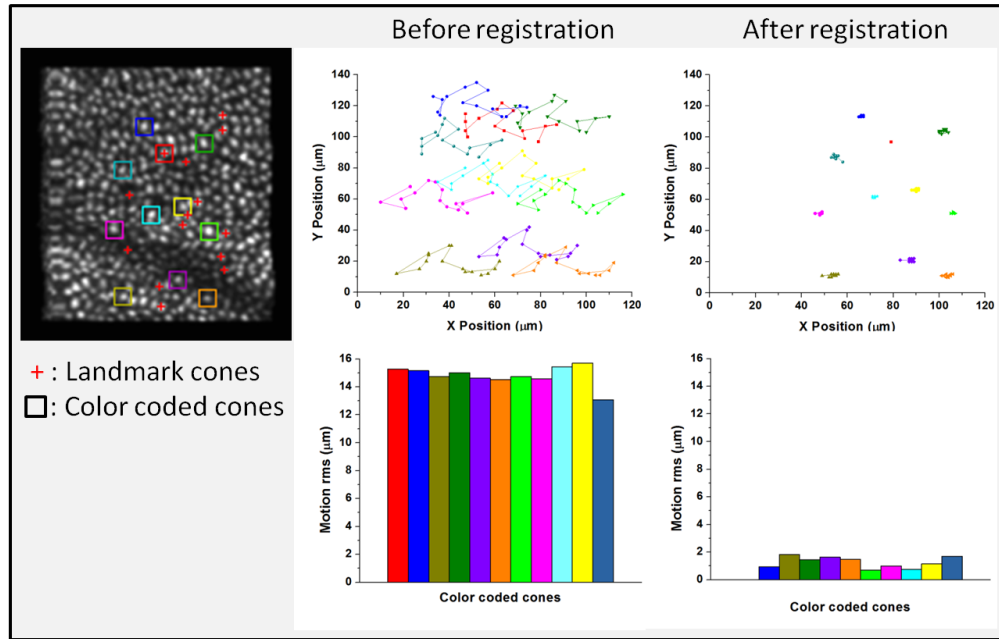

Fig. 8. (left column) An *en face* frame from the volume movie at 3° temporal to the fovea. Red crosses mark the locations of 14 landmark cones used for registration. Color-coded squares mark the locations of 11 cones that were tracked during the volume video. 10 of the cones were randomly selected but present in all frames, while one was intentionally selected as a landmark cone (red). (center column) Traces of *en face* position of the 11 cones and RMS magnitude of each cone (landmark cone is red) are shown without registration. (right column) Traces of *en face* position and RMS magnitude of the same 11 cones are shown with registration/dewarping. Registration/dewarping used 13 strips (14 landmark cones).
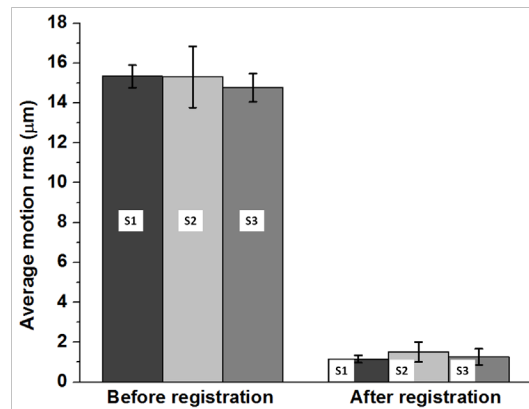

Fig. 9. Lateral motion of the retina during UHR-AO-OCT image acquisition before and after registration/dewarping. Averages are shown for each subject (S1, S2, and S3). Each bar represents the average RMS of five cones selected in volume videos at 3°. Error bars represesent ± 1 standard deviation of the five cone measurements.

Figure 9 summarizes the registration/dewarping algorithm's performance across the three subjects for the 3° volume movies. Shown is the average motion RMS before and after registration/dewarping, which were determined from tracking five cones in each video. The three subjects exhibited similar levels of motion RMS of about 15 μm (prior to registration/dewarping), and the registration algorithm performed similarly regardless of subject, reducing the RMS on average to 1.3 μm. In general, the registration algorithm reduced the motion RMS by more than an order of magnitude (15 μm to 1.3 μm).

3.3. Cone OS length measurements

Once the cones were stabilized in *en face* views using the strip-based registration/dewarping methodology, corresponding cross-sectional movies of individual cones were extracted for further analysis. Figure 10 and Media 4 show the cross-section of six representative cones, the two right most being landmark cones. The media file reveals motion is still present between frames, but the full amplitude of the motion remains less than the width of a cone. Based on repeated measurements of the cone OS length (one measurement per each frame of the video), the average length and standard deviation for the six cones in Fig. 10 are 27.7 ± 0.6 μm (yellow), 26.9 ± 0.8 μm (blue), 29.1 ± 0.5 μm (green), 27.6 ± 0.5 μm (violet), 27.4 ± 0.6 μm (red, left landmark cone), and 28.9 ± 0.7 μm (red, right landmark cone). Note that for the yellow- and green-bordered cones, the presence of additional reflections causes some ambiguity as to which one correctly corresponds to the PTOS. Here we assumed the third reflection from the top was the PTOS.
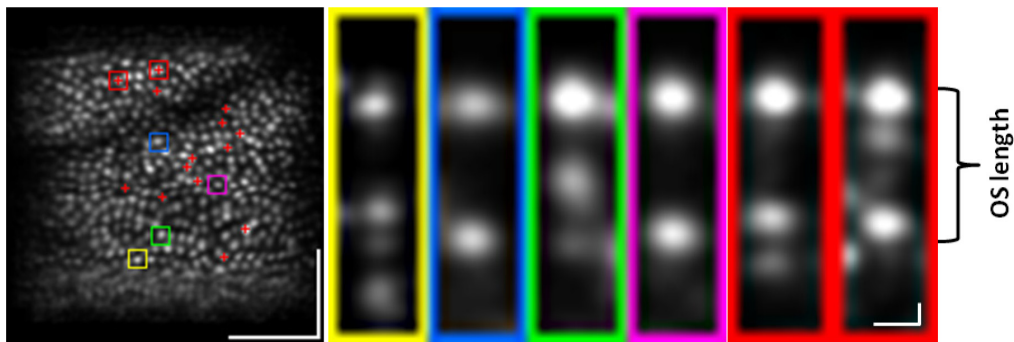

Fig. 10. (left) Averaged e*n face* image of S3 at 3° temporal to the fovea after registration and (right) cross-sectional images of individual cones. *En face* locations of cross-sectional images are marked by colored squares (yellow, blue, green, violet, red). Landmark cones used for registration are marked with red crosses. The cross-sectional cone images shown in red are landmark cones. Media 4 shows the registered *en face* UHR-AO-OCT movie from which the average image was computed along with cross-sectional movies of the six cones selected. Scale bars on the projection and cross-sectional images indicate 50 μm and 5 μm, respectively.

Following the same measurement protocol, Fig. 11 shows OS length measurements of 36 cones across the three subjects (12 cones per subject) and three retinal eccentricities (12 cones per location). The RMS error bars of Fig. 11 (left) represent the variation in repeated OS length measurements of the same cone over the volume movie (intra-cone variability). For comparison, the RMS error bars of Fig. 11 (right) denote the variation in OS length for the four cones at the same retinal eccentricity and subject (inter-cone variability).
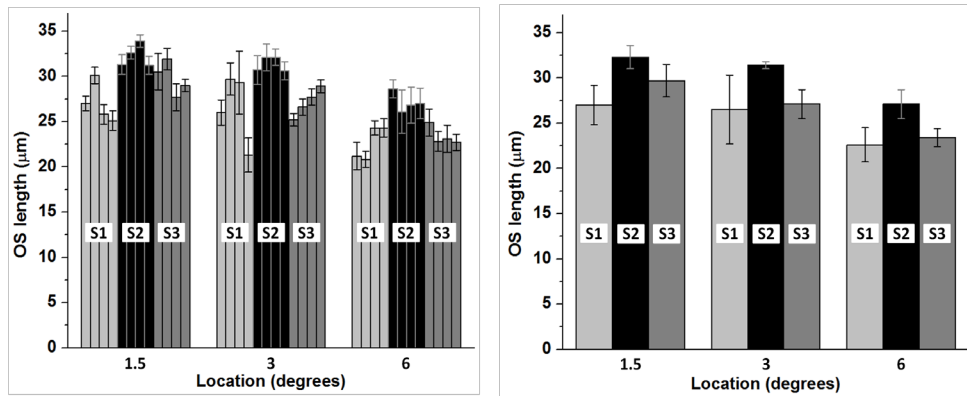
Fig. 11. UHR-AO-OCT measurement of cone OS length. (left) Average OS length of individual cones at 1.5°, 3°, and 6° temporal to the fovea and for the three subjects (four cones per eccentricity per subject). Error bars represent ± 1 standard deviation of 10 to 15 (14.2, on average) OS length measurements (intra-cone variability). (right) Average OS length of four cones at the same retinal eccentricity and same subject. Error bars represent ±1 standard deviation of OS length measurements over the four cones (inter-cone variability).

4. Discussion

In this study we assessed the ability of UHR-AO-OCT to image individual cone photoreceptors in three dimensions and in time. Our approach to mitigate eye motion artifacts was to integrate a high-speed (125K lines/s) spectrometer into UHR-AO-OCT followed by a novel registration/dewarping post processing methodology. Effectiveness was assessed using volume movies of 0.5°x0.5° retinal patches that contained cones over a range of sizes and packing densities in three healthy subjects.

4.1. Cone spacing

Power spectra of the *en face* views revealed a faint, but clear ring of concentrated power centered about zero spatial frequency. The ring was present for the three retinal eccentricites and three subjects examined (example, Fig. 4). To determine whether the ring radius corresponded to the fundamental spatial frequency of row-to-row cone spacing, we compared the corresponding spacing to cone spacing as reported in the literature using AO-SLO and histology (see Fig. 5). The consistency of the UHR-AO-OCT measurements to the literature provides supportive evidence that the observed ring in the power spectra is likely Yellott's and that UHR-AO-OCT is capable of resolving individual cones *en face* over the range of retinal locations imaged.

4.2. Motion artifacts and image registration

Even with ultrahigh speed imaging (125K A-line/s) and small volumes (150x150 px), the volume acquisition rate of UHR-AO-OCT is up to six times slower than the frame rate of AO-SLO systems (~6 Hz compared to ~30 Hz). Likely more relevant is the fast scan rate (B-scans/s) of UHR-AO-OCT that is up to 19 times slower than the line rate of AO-SLO (1.2 ms compared to 64 µs). These slower rates manifest as increased motion artifacts and warp in UHR-AO-OCT projection views as compared to AO-SLO images. To illustrate this difference, consider the number of fast scans that can be acquired in 10 ms, the maximum duration for which retina motion (under normal steady fixation) does not typically exceed the diameter of a cone photoreceptor (i.e., retina motion is effectively frozen) [38,30,39,27]. For this duration, just eight UHR-AO-OCT B-scans are acquired compared to 156 AO-SLO line scans.

Based on this difference in acquisition speeds, it is not surprising that AO-SLO images can be registered using large strips of the image for motion estimation and dewarping [20,22–

25], whereas UHR-AO-OCT volumes demand that smaller strips of 10-15 B-scans be used. Additional transformations of the strips, such as stretching, shrinking, and shearing, were employed based on our observation that the small strips suffer from motion artifacts other than relative translation. While our narrow sub-strip methodology is effective, it does come at a cost. Specifically in its current implementation, it requires manually tracking of landmark cones through the volume video. Such manual tracking is slow and tedious. As an example, tracking 10 landmark cones through 15 volumes typically takes 30 minutes for a trained specialist.

For the three subjects imaged in this study, the amplitude of lateral retinal motion was approximately 50 μm (10 arc min) peak-to-valley and 15 μm (3 arc min) RMS across the volume movies (see Figs. 8 and 9). This motion amplitude falls well within the range of normal steady fixation consisting of tremor, drift, and microsaccades [17]. While the 15 μm RMS motion may be considered small, it results in substantial artifacts at the level of cones, which are only a few microns in diameter. This makes visual tracking of individual cones exceedingly difficult in the volume videos (see for example Media 2). Our registration/ dewarping algorithm effectively reduced this motion by approximately 12 times, resulting in a residual motion of 1.3 μm RMS for non landmark cones that is noticeably less than the width of an individual cone. For the landmark cones, we did not quantify their residual lateral motion, which would have revealed any error in the manual tracking process. Nevertheless, visual comparison of the cross-sectional videos of landmark and non landmark cones in Fig. 10 (Media 4) clearly shows the landmark cones to be more stable. Hence performance of our registration/dewarping methodology is likely limited by factors unrelated to the manual portion of the method. The residual motion of 1.3 μm RMS for non landmark cones was found sufficient for aligning and averaging images, and identifying and tracking cones (see Figs. 6, 7 and 10). As the subjects tested in our experiment are representative of patients with normal steady fixation, our approach should be effective over a large portion of the population.

4.3. OS length measurements

The vast majority of cones imaged at 1.5° and 3° retinal eccentricity and a smaller but still appreciable fraction at 6° retinal eccentricity generated two distinct reflections that straddled the cone OS, one at the IS/OS junction and the other at the OS posterior tip. The distance between these was used as the OS length. Examples include the second and fourth cone cross sections (from the left) in Fig. 10. A small fraction of cones generated additional reflections within the OS, immediately posterior of the POST, or both. Examples include the first and third cone cross sections (from the left) in Fig. 10. This subset of cones with additional reflections is consistent with Pircher *et al* who reported similar findings using an *en face* scanning OCT system. Additional reflections immediately adjacent to either OS tip increased the uncertainty of locating the OS borders and thus our determination of the OS length. It is unclear the source of these additional reflections and why only a small fraction of cones generate them. Perhaps these additional reflections occur at locations where the regular arrangement of the OS discs is disturbed. The source of additional bright reflections immediately posterior to the OS tips is also unclear, but may be attributable to disc shedding as for example reflections from discs that have been recently phagocytosed by the underlying RPE cells. While we can only speculate at this point as to the source of both types of reflections, the UHR-AO-OCT method presented here provides a direct means to which we can test these hypotheses by following the course of individual bright reflections (internal and external to the cone OS) over days as the cones undergo continued renewal and disc shedding.

Previous reports of OS length measurements using conventional OCT (without AO) lack the lateral resolution to individuate cones and therefore are limited to measuring the bulk thickness of the OS layer, as opposed to that of single cones. As an appropriate comparison then, UHR-AO-OCT OS length measurements averaged over all subjects (Fig. 11 (right), 29.6

± 2.7 μm at 1.5°, 28.3 ± 3.1 μm at 3°, and 24.4 ± 2.4 μm at 6°) are 5 μm and 3 μm shorter than Sirinivasan *et al.* [40] reported at 1.5° and 3° respectively, who used UHR-OCT for OS length measurements (35 μm at 1.5° and 31 μm at 3°). McAllister *et al.* [41] reported their OS length measurements of 167 normal subjects using a clinical SD-OCT instrument at 1.5°, 3°, and 6° temporal to the fovea as 30.0 ± 5.3 μm, 25.8 ± 4.8 μm, and 22.3 ± 5.9 μm, respectively. Our measurements show good agreement with this large population study. Interestingly using a clinical OCT system (Heidelberg Spectralis), OS length measurements on the three subjects in this study were approximately 4 μm shorter (S1 = 23 μm, S2 = 27 μm, S3 = 24 μm at 3°) than the corresponding UHR-AO-OCT measurements in Fig. 11 (right), which points to a systematic error in one of the measurements.

As a final step, we analyzed the sensitivity of our UHR-AO-OCT methodology to detect differences among cone OS lengths, based on the measurements used in Fig. 11. From a volume video, each cone's length was measured 10 to 15 times (14.2, on average). We assume the standard deviation of these measurements, $\sigma_{intra-cone}$, represents a noise limit, the smallest length difference that can be observed with a single measurement. $\sigma_{intra-cone}$ is calculated by taking the square root of the average measurement variance for each cone in the study (36 cones), weighted by number of measurements (10 to 15 measurements). $\sigma_{intra-cone}$ is 1.41 μm, well below the 3 μm axial (optical) resolution of the UHR-AO-OCT instrument. Similarly, we assume the standard deviation of average measured OS lengths from our single (<0.5 deg) patches of retina, $\sigma_{inter-cone}$, represents true local OS length variability. $\sigma_{inter-cone}$ is calculated by taking the square root of the average length variance among cones in a retinal patch (9 patches total–3 subjects, 3 eccentricities each), weighted by number of cones (4 cones per patch). $\sigma_{inter-cone}$ is 1.55 μm. Given that $\sigma_{inter-cone} > \sigma_{intra-cone}$, it suggests that differences in OS length within small patches of retina can be detected using UHR-AO-OCT.

To quantify the extent to which these differences are detectable, we undertook two statistical tests. First, for each of the nine retinal patches (3 subjects, 3 eccentricities), we used ANOVA on groups of repeated length measurements (1 group per cone), testing the null hypothesis that the four cones in each patch had the same length. In all nine cases, the null hypothesis was rejected ($\alpha = 0.05$), with p values ranging from 0.000 to 0.006. Thus, differences in OS length were detected at all retinal locations.

Second, as the ANOVA utilized repeated measurements (~14 per cone), we sought to determine the minimum number of measurements required to distinguish two OS lengths. Letting N represent the number of measurements, and starting with $N = 1$, we incremented N and computed probability density functions for the t-distribution using N and degree of freedom, $d_f = N - 1$. Also, for each N we computed a t-statistic, $t = \sigma_{inter-cone}/(\sigma_{intra-cone}/\sqrt{N})$, and determined a corresponding probability p using the probability density function. We determined that no more than five measurements were required to detect a difference of $\sigma_{inter-cone}$ (1.55 μm) with 95% confidence.

In summary, our cone length analysis demonstrates that UHR-AO-OCT is sufficiently sensitive to measure real length differences between cones in the same 0.5 deg retinal patch, and requires no more than five measurements of OS length to achieve 95% confidence. Such exquisite sensitivity to cellular length rivals histology, but has the added benefit of being accomplished in the living human eye. While an AO flood illumination system has recently demonstrated even better sensitivity (139 nm) [26], that method is limited to measuring changes in the OS length, not absolute length as accomplished here, assuming OS has a constant and known refractive index ($n_{os} = 1.43$). At the very least, UHR-AO-OCT provides a vastly more detailed description of cone morphology than is possible using commercial OCT.

5. Conclusion

Results presented here demonstrate the feasibility of UHR-AO-OCT to image individual cone photoreceptors in three dimensions and to track their reflectance over time. Critical to this success was the use of high speed image acquisition (125 KHz) and a novel registration/

dewarping methodology. Image registration and OS length measurements were found to surpass the 3D optical resolution of the UHR-AO-OCT instrument.

Acknowledgments